Clinical Anatomy 32:361–368 (2019)

ORIGINAL COMMUNICATION

Computerized Anatomy of the Distal Radius and its Relevance to Volar Plating, Research, and Teaching

DOMINIC GEHWEILER,[1] TEUN TEUNIS ,[2*] VIKTOR VARJAS,[1] DIRK KERSTAN,[3] BOYKO GUEORGUIEV,[1] LUKAS KAMER,[1] AND HANSRUDI NOSER[1]

[1]*AO Research Institute Davos, Davos, Switzerland*
[2]*Plastic Surgery Department, University Medical Center Utrecht, Utrecht, The Netherlands*
[3]*DePuy Synthes, Zuchwil, Switzerland*

Distal radius fractures are common and fracture patterns and fixation can be complex. Computerized anatomy evaluation (CAE) might offer non-invasive and enhanced anatomy assessment that might help with implant selection and placement and screw length determination. Our goal was to test the accuracy of two CAE methods for anatomical volar plate positioning and screw lengths measurement of the distal radius. We included 56 high-resolution peripheral quantitative computed tomography scans of intact, human distal radii. Plates were placed manually onto 3D printed models (method 1), which was compared with automated computerized plate placement onto the 3D computer models (method 2). Subsequently, screw lengths were determined digitally for both methods. Screw lengths evaluations were compared via Bland–Altman plots. Both CAE methods resulted in identical volar plate selection and in anatomical plate positioning. For screw length the concordance correlation coefficient was ≥0.91, the location shift ≤0.22 mm, and the scale shift ≤0.16. The differences were smaller than ±1 mm in all samples. Both CAE methods allow for comparable plate positioning and subsequent screw length measurement in distal radius volar plating. Both can be used as a non-invasive teaching environment for volar plate fixation. Method 2 even offers fully computerized assessments. Future studies could compare our models to other anatomical areas, post-operative volar plate positioning, and model performance in actual distal radius fracture instead of intact radii. Clin. Anat. 32:361–368, 2019.

Key words: radius; anatomy; tomography

INTRODUCTION

Operative fixation of distal radius fractures is a common surgical procedure comprising a variety of different treatment options such as various plating techniques and k-wire fixation (Chung et al., 2009; Horst and Jupiter, 2016).

Osteosynthesis via plate fixation requires anatomical implant positioning with a plate and several screws to be correctly placed at the radial shaft and distally to obtain subchondral support. Technical aspects include adequate reduction, plate positioning, plate size, and

*Correspondence to: Teun Teunis, MD, PhD, University Medical Center Utrecht, Heidelberglaan 100, 3584 CX, Utrecht, The Netherlads.
E-mail: teunteunis@gmail.com

Grant sponsor: This work was funded by DePuy Synthes, Zuchwil, Switzerland.
The authors declare no potential conflicts of interest with respect to the research, authorship, and/or publication of this article.

Received 16 October 2018; Revised 26 November 2018; Accepted 2 December 2018

Published online 23 December 2018 in Wiley Online Library (wileyonlinelibrary.com). DOI: 10.1002/ca.23320

screw length. Overestimation of the screw lengths might result in soft tissue problems, such as tendonitis and tendon rupture, whereas too short screws might compromise implant anchorage, particularly when associated with osteoporosis (Davis and Baratz, 2010; Handoll and Elliott, 2015; Synek et al., 2016).

Computerized techniques could be used for non-invasive extended anatomy evaluations. In particular, they could be used to repetitively assess anatomical features relevant to volar plating of the distal radius during anatomy labs without the use of post mortem specimens.

Several computerized methods have been described. Computed tomography (CT) was used to assess detailed fracture configuration (Teunis et al., 2016). Computer-assisted planning and 3D printing technologies were useful for virtual planning of distal radius osteotomies, as well as for prebending of fixation plates used in corrective osteotomies of pediatric forearm malunions (Leong et al., 2010; Storelli et al., 2015; Vlachopoulos et al., 2015). Computer-assisted fracture reduction was helpful in artificial tibia models, CT models of the proximal humerus and of the mandible (Furnstahl et al., 2012; Buschbaum et al., 2015; Voss et al., 2016). High-resolution peripheral quantitative computed tomography (HR-pQCT) represents an imaging source that can be used to obtain image data with an image resolution about 100 μm and quantitative bone information with the gray values given in volumetric bone mineral values (vBMD), particularly useful for detailed assessment of cortical and trabecular bone regions (Genant et al., 2008; Burghardt et al., 2011).

Accurate 3D printed and digital models can help with non-invasive implant selection and positioning, and screw length determination. Our goal was to test the accuracy of two computerized anatomy evaluation (CAE) methods at anatomical volar plate positioning and screw length measurements of the distal radius.

METHODS

Image Data

Fifty-six anonymized high-resolution peripheral quantitative computed tomography (HR-pQCT) scans of intact, human distal radii were taken from the image database of the AO Research Institute Davos, Switzerland, registered at the "Eidgenössischer Öffentlichkeits- und Datenschutzbeauftragter" (EDÖP, No. 200700006) Bern, Switzerland. The HR-pQCTs consisted of 49 right and 7 left image data samples from donors aged at death 66 (SD 18.4) years; range: 25–93 years; (28 female samples: age 65 (SD 20.3) years; 28 male samples: age 67 (SD 16.5) years). This study was approved by the institutional internal review board, based on the approval of the specimens' delivery by Science Care Ethics Committee. All donors have given their informed consent inherent within the donation of the anatomical gift statement during their lifetime.

The image data were acquired from fresh-frozen, post mortem forearm specimens (Science Care, Phoenix, Arizona, USA). The specimens were defleshed, kept vacuum-packed and stored at −20°C until use. Prior to HR-pQCT imaging they were thawed to room temperature. The acquisition protocol comprised scanning of the distal radius at a maximum length of 16 cm using a HR-pQCT scanner (XtremeCT™, Scanco Medical, Brüttisellen, Switzerland) with phantom calibration as described by Kamer et al. (2016). The image data, available in Digital Imaging and Communications in Medicine (DICOM) file format, were checked using standard, orthogonal slices prior to processing to exclude potential unreported alterations such as unidentified bone disease and previous fracture.

Computer Models

Fifty-six computer models of the distal radius, corresponding to the above mentioned HR-pQCT data, were also taken from the image database. They were generated using a standard semi-automated segmentation procedure according to a technique described by Noser et al. (2011).

Implants

Titanium volar locking plates for distal radius fixation with variable angle locking holes and elongated combi holes (2.4 mm Variable Angle LCP Two-Column Distal Radius Plate, Synthes GmbH, Oberdorf, Switzerland) for the left and right side of the distal radius were available in narrow (19.5 mm), normal (22 mm), and wide (25.5 mm) head size configurations. In addition, narrow, normal and wide computerized plate templates were available in STL file format.

Soft- and Hardware Framework

We used the software environment Amira [version 6.0.0, FEI (Field Emission Inc.), Hillsboro]. Amira is a commercially available and extendable software for scientific visualization and analysis, as well as for presentation of medical imaging data. The software was extended by custom TCL scripts and modules programmed in C++ language and combined with ITK (Insight Segmentation and Registration Toolkit, U.S. National Library of Medicine), which is an open-source software system for medical image processing.

CAE Methods for Plate Positioning and Screw Length Measurements

Method 1 (M1)—plate positioning and screw length measurements via 3D printed models - About 56 above mentioned distal radius models were subjected to an EOSINT P 760 Selective Laser Sintering system (EOS GmbH Electro Optical Systems, Munich, Germany) with a 0.12 mm layer thickness to produce 56 3D printed distal radius models from polyamide material.

An appropriate sized titanium volar locking plate was selected for each of the 3D printed models of the distal radius and manually positioned onto its volar

region by a trained surgeon (TT). The position of each plate was checked, particularly with regard to the shaft axis and the Watershed line. This line marks the distal ridge of the pronator fossa. It serves as a distal margin for volar plating to minimize flexor tendon injuries. The plates were temporally fixed on the 3D printed models using hot-setting glue (Fig. 1A) and scanned using a clinical CT scanner (Siemens SOMATOM Definition AS scanner, Siemens AG, Munich, Germany) with a $0.34 \times 0.34 \times 0.2$ mm image resolution and a V80u convolution kernel. Standard semi-automated CT image segmentation was then performed in Amira to obtain a computer model of the distal radius with integrated volar plate (Fig. 1B). The corresponding virtual plate templates were registered to the computer models of the distal radius using an iterative closest point (ICP) algorithm allowing for rigid motion (Fig. 1C). Thus, the virtual plate template was positioned according to expert placement.

The screw lengths were automatically calculated for each of the variable angle screw holes VA1–VA6 and the combi holes C1–C3 (Fig. 2C). The middle VA hole of the wide plate was not used for measurements, because it had no corresponding hole on the normal and narrow plates (Fig. 2C). The measurements for VA1–VA4 and C1–C3 were performed in a neutral screw position with respect to the nominal axis of the screw hole, that is, without a specific screw angulation (Fig. 2A). For the two holes VA5 and VA6 (Fig. 2C) located near the styloid process screw lengths were determined with the first screw manually oriented more distally toward the styloid process and the second one oriented parallel to first screw direction. These two measurements were performed in a maximum screw angulation of 15° (Fig. 2B) and labeled as VA5a and VA6a for presentation of the results later.

During screw length measurement, the diameter of each screw was taken into account in a way such that the shortest distance to the outer bone surface measured around the wall of the drill hole was chosen to ensure no screw protrusion outside the bone. All measurements were compared with M1 that served as the reference method.

Method 2 (M2)—plate positioning and screw length measurements via 3D computer models The principal axis of each distal radius model was computed in Amira and aligned to the axis of the global coordinate system to facilitate virtual plate positioning. Virtual plate templates were pre-aligned via definition of three landmarks on the surfaces of the computer models of the distal radii in this system (Fig. 3A), corresponding to plate template landmarks. Based on the predefined landmarks, a point-based rigid pre-alignment transformation was computed. Starting from the initial plate and bone positions, an automatic plate fitting procedure was

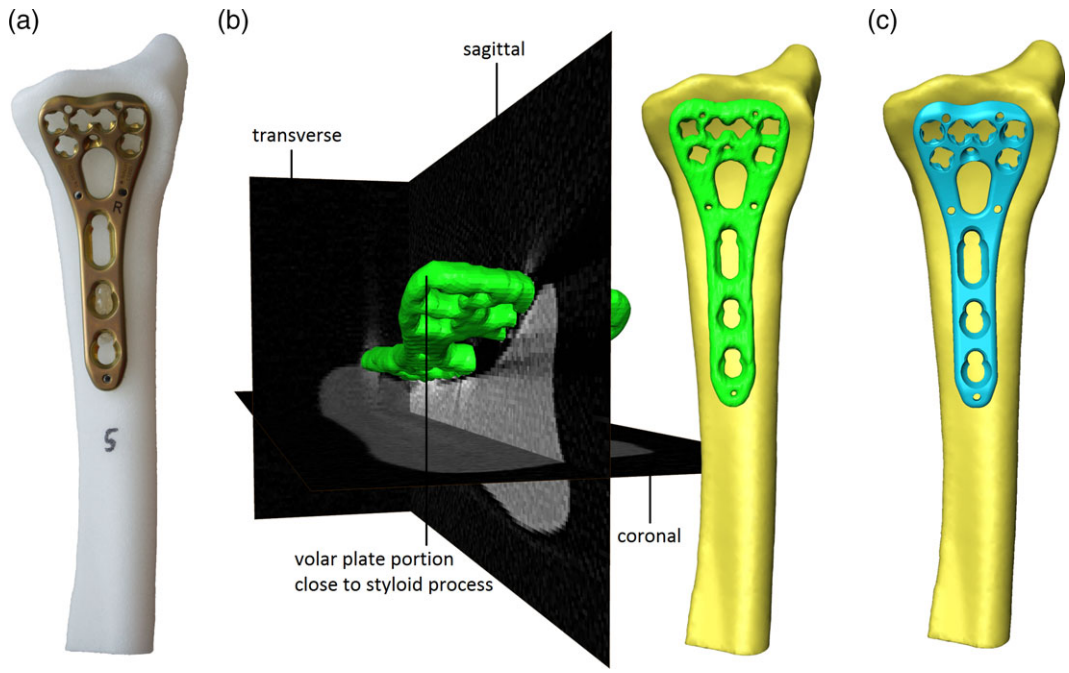

Fig. 1. Modeling workflow of M1: A: a right volar plate fixed on an exemplified 3D printed model of the distal radius; B: left: CT scan with orthogonal views of a 3D printed distal radius and a semi-automated segmented 3D model of the plate (green) (note also CT artifacts due the metallic implant), right: computer model of a right distal radius (yellow) with attached volar plate (green) after CT scanning and image segmentation; C: computer model of the right distal radius (yellow) and the registered virtual plate template (blue). [Color figure can be viewed at wileyonlinelibrary.com]

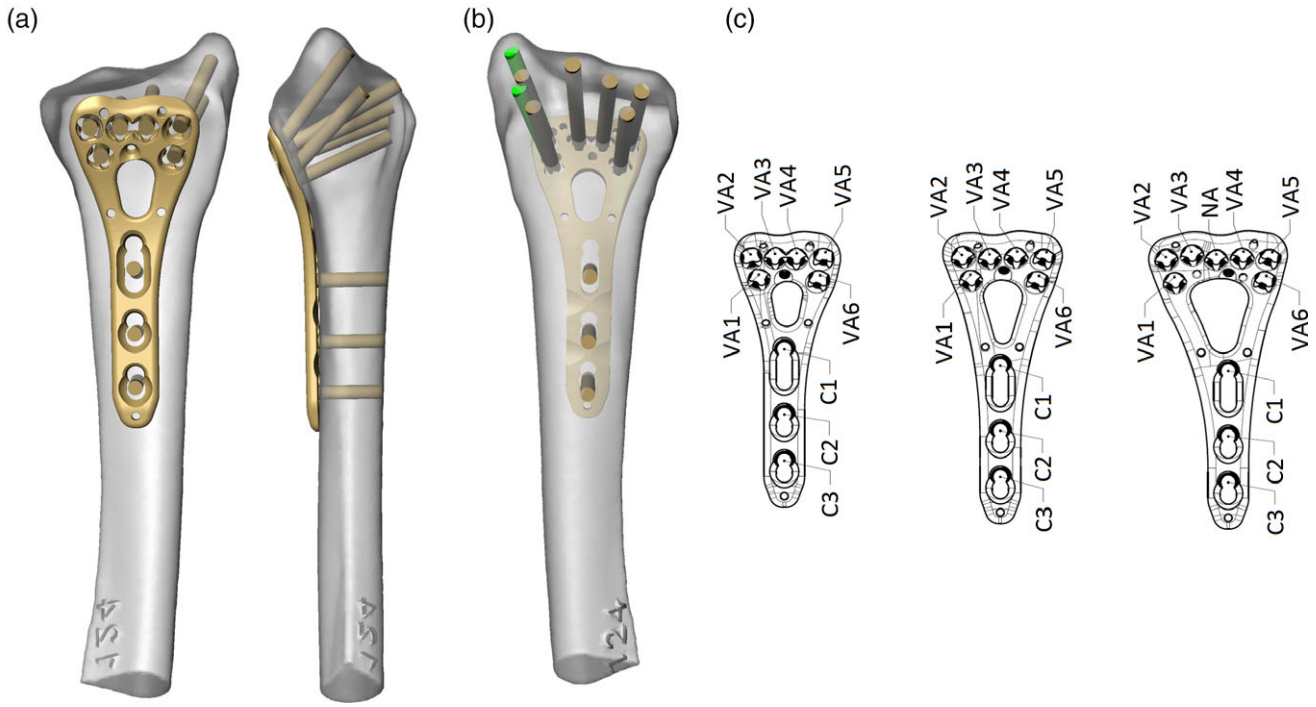

Fig. 2. Computerized screw length measurements: A: volar plate with screws in neutral positions without specific screw angulations (volar and lateral views), B: the two parallel screws (green), manually oriented more distally toward the styloid process with 15° angulation (dorsal view), C: labeling of the screw hole positions in narrow, normal and wide plates. [Color figure can be viewed at wileyonlinelibrary.com]

performed to ensure an optimal fit between the plate and the bone while avoiding plate–bone intersections. The optimization was performed using the Euclidean distance transform (cost image) of the bone model which penalized plate–bone intersections and positions away from the bone surface. For each evaluated position the shortest plate vertex distances from the bone were summed up using the cost image. The position corresponding to the lowest cost was chosen. For each distal radius sample an efficient heuristic search algorithm systematically evaluated approximately 1 million different plate positions within 2 s. The optimization was performed with a user-defined fineness and range of rotation angles and translations (around and along the three axes) with 50 randomly chosen plate rotation centers for each evaluated rotation angle. All virtually positioned plates were checked by a trained surgeon (TT) (Fig. 3B).

Accordingly, the screw length measurements were performed as described above.

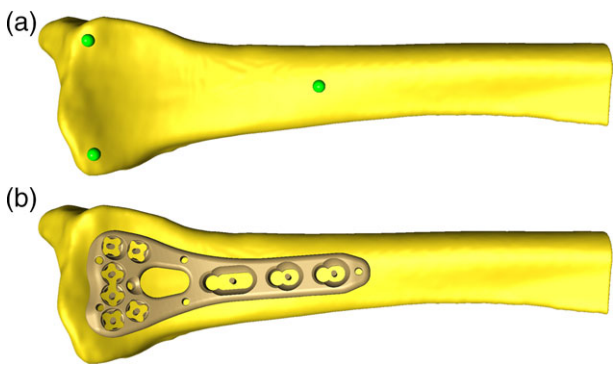

Fig. 3. Virtual plate positioning onto the volar side of a computer model of the distal radius: A: manually placed landmarks (green) used for pre-alignment of the virtual plate template, B: final position of the plate template after running the optimization algorithm. [Color figure can be viewed at wileyonlinelibrary.com]

Statistical Analysis

We report screw length median, IQR, means, and standard deviations. Assessment of concordance of intra-individual measurement values included scatter plots of the measured points created using MATLAB (Version R2015b, The MathWorks, Inc., Natick), Bland–Altman plots, and the calculation of concordance correlation coefficients as described by Koch and Sporl and Bland and Altman (Bland and Altman, 1986; Koch and Sporl, 2007). Scatter plots included the identity line ($x = y$), mean values, the orthogonal, the $y(x)$, the $x(y)$, and the structural regression (sStruct) lines (Fig. 4).

RESULTS

For M1 and M2 identical plates were selected and anatomically placed as defined by a trained surgeon (TT). In Table 1 descriptive statistics were presented for the nine screw holes of the volar plates.

The median screw lengths for the shaft screws increased from the proximal position C3 to the distal position C1 and were comparatively smaller than the variable angle screw lengths. The medians of the VA screw lengths for the middle screw positions (VA3 and VA4) were higher than those for the ulnar screws and the medians of the VA screw lengths for the ulnar screws were higher than those for radial screws.

The comparison of the screw length of M1 versus M2 exhibited a high concordance correlation coefficient (ccc ≥ 0.91) for all screws. For the shaft screws it was ≥0.98. The location shift was ≤0.22 mm and the scale shift was ≤0.16. The 95% confidence interval (95 CI) of the differences in measured screw length between M1 and M2 for all screws was (−1.34 mm ≤ 95 CI ≤ 1.70 mm); for the shaft screw it was (−0.53 mm ≤ 95 CI ≤ 0.76 mm).

In Figure 4 screw length evaluations were exemplified for screw hole position C1 and comparison between M1 and M2. The median screw length measurement with both methods was 13.1 mm; the ccc was 0.99 and the 95 CI was (−0.44 mm ≤ 95 CI ≤ 0.48 mm). The differences between M1 and M2 were smaller than ±1 mm in 100% of the measurements.

All statistical values from the comparisons between M1 versus M2 for all screws were given in Table 2.

DISCUSSION

Plate positioning and determination of the screw length are essential parts of numerous operative fracture fixation procedures. Volar plating of the distal radius is a common, however, demanding surgical procedure. The operative technique requires the Watershed line, radial metaphysis, articular realignment, type, number, location of plates, and screws to be taken into account. So far, plate positioning and screw length measurements and their evaluation have been demanding tasks when using a traditional evaluation setup.

Our main consideration was that computerized techniques could be used for safe and extended anatomy evaluations while offering non-invasive, non-destructive, and repetitive assessments; that is, as an alternative to standard evaluations such as used within intraoperative setups or during anatomy labs with post mortem specimens. When transferred to fracture fixation setup of the distal radius, CAE could be utilized to assess anatomical features relevant for volar plating of the distal radius. Further, we consider CAE to be a safe and effective procedure for the following reasons: They allow for data (e.g., image data or database information) to be reused and therefore the amount of body donations to be reduced (Messmer et al., 2007; Chen et al., 2018; Lee et al., 2018), do not expose people to harmful incidents [e.g., needlestick injuries (Chambers et al., 2015)] and provide a new learning environment (Hopkins et al., 2011). Since performed virtually, all procedures can be constantly repeated and adapted, if required.

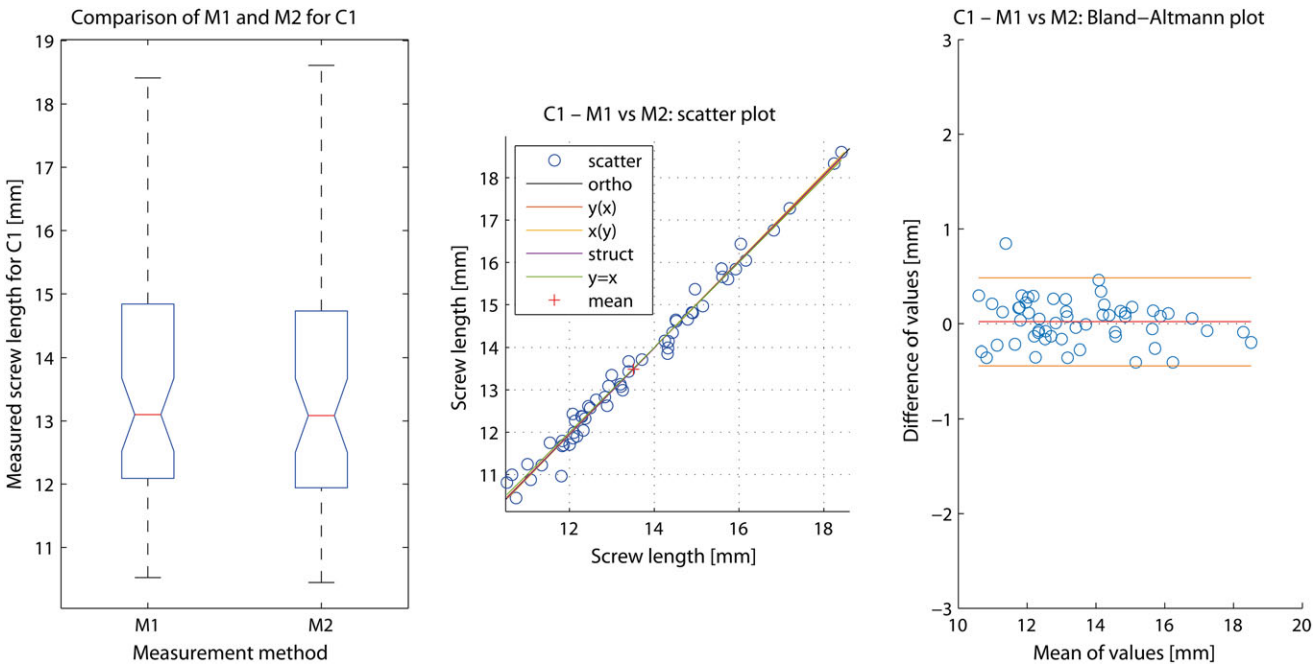

Fig. 4. Box plots (left), scatter plot (middle) and Bland–Altman plot (right) for C1 when comparing M1 versus M2. [Color figure can be viewed at wileyonlinelibrary.com]

TABLE 1. Screw Lengths of Method 1 and 2

Method 1	VA1	VA2	VA3	VA4	VA5a	VA6a	C1	C2	C3
Median	19.8	20.5	22.2	21.5	18.7	17.8	13.1	12.1	11.9
IQR	3.6	3.1	2.7	1.9	2.8	2.6	2.7	2.6	2.6
min	16.1	17.0	18.9	18.4	15.1	14.7	10.5	9.8	9.8
max	25.5	26.1	26.7	25.4	23.5	22.4	18.4	17.3	16.9
Method 2									
Median	19.6	20.2	22.3	21.1	18.5	18.0	13.1	12.1	11.9
IQR	3.9	3.5	3.1	1.5	2.1	2.4	2.8	2.6	2.3
min	16.4	16.5	18.4	19.0	14.8	15.0	10.4	10.0	10.1
max	25.6	26.0	27.2	24.6	22.9	21.8	18.6	17.4	16.5

Screw length determined for the variable angle screws positions VA1–VA4 with a 0° angulation, for the variable angle screws positions VA5a–VA6a with a 15° angulation, and cortical screws C1–C3 with a 0° angulation.

TABLE 2. Differences in Screw Length Between Method 1 and 2

	VA1	VA2	VA3	VA4	VA5a	VA6a	C1	C2	C3
Mean (mm)	0.18	0.16	0.04	0.16	0.22	0.14	0.02	0.05	0.12
Std (mm)	0.77	0.63	0.52	0.61	0.55	0.44	0.24	0.25	0.33
Upper (mm)	1.7	1.41	1.06	1.35	1.29	1.01	0.48	0.54	0.76
Lower (mm)	−1.34	−1.08	−0.98	−1.04	−0.85	−0.73	−0.44	−0.44	−0.53
<±1 mm (%)	76.8	87.5	94.6	94.6	94.6	98.2	100.0	100.0	100.0
ccc	0.95	0.96	0.97	0.91	0.95	0.96	0.99	0.99	0.98
sStruct	0.98	0.97	1.02	0.84	0.92	0.91	1.02	1.01	0.96

VA, variable angle locking screw hole; C, cortical screw hole; Std, standard deviation; ccc, concordance correlation coefficient; sStruct, structural regression.

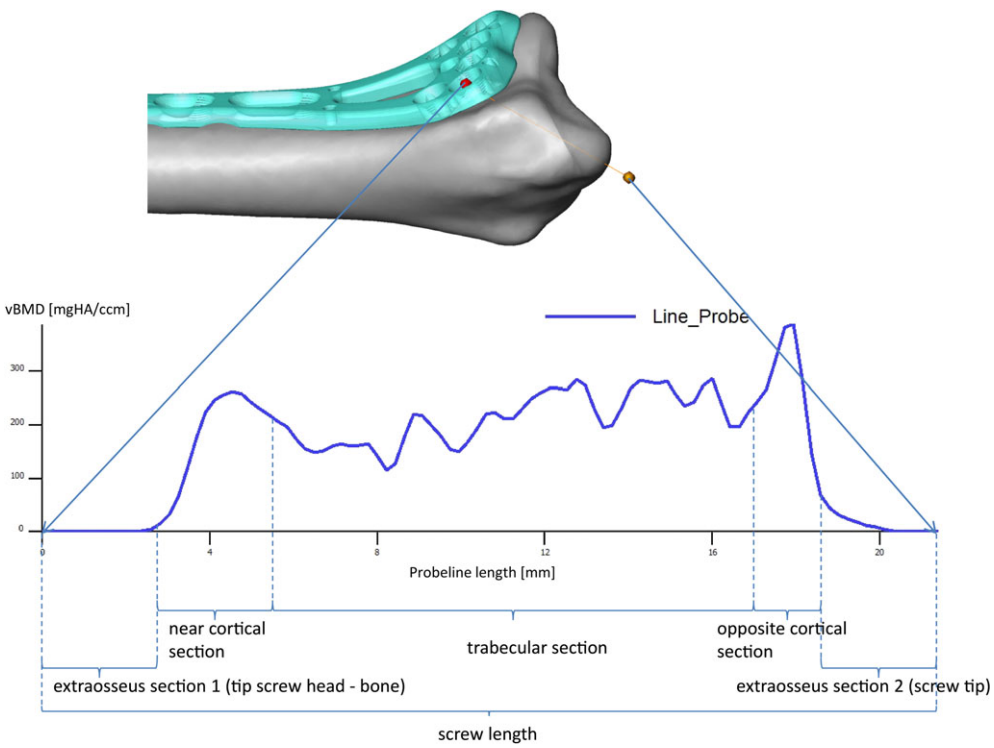

Fig. 5. Example for additional screw HR-pQCT measurements (gray values given in vBMD) at a given screw position (VA5) when using virtual methods. [Color figure can be viewed at wileyonlinelibrary.com]

Moreover, CAE provided information that allowed for new measurements and that are impossible to perform using a standard measurement setup (also see Fig. 5).

The CAE methods used were based on 3D anatomy records, that is, 56 HR-pQCT scans of the distal radius and their 3D computer models. HR-pQCT imaging is a tomographic imaging source (Boutroy et al., 2005; Davis et al., 2007; Melton et al., 2007; Mueller et al., 2009), that provides 3D image data with a high resolution of 82 μm, including data for vBMD. In contrast to CT, HR-pQCT allows improved identification of trabecular and cortical structures, mainly because of its higher image resolution (Genant et al., 2008). Yet, CT imaging remains a diagnostic mainstay to assess complex clinical cases and it cannot provide such detailed information.

Starting from intact data samples, anatomical plate positioning was a key task to be accomplished prior to screw lengths measurement. In the first CAE method, we applied a manual plate positioning procedure to place volar plates onto physical models of the distal radius that were manufactured via 3D printing. Plate positioning was checked by a trained surgeon, particularly with regard to the axial orientation and consideration of the Watershed line. Neither manual plate bending nor elastic fitting of the virtual plate templates to the distal radius models was needed. However, as CT-imaging was used in method 1 the accuracy and precision of the measurements can be limited by the CT image resolution, as errors have about the same size as the scan resolution (Noser et al., 2011). The second CAE method even allowed for fully computerized evaluations.

To characterize intra-individual concordance or intraclass correlation, the concordance correlation coefficient ccc was computed. Values for ccc between 0.81 and 1 represent a nearly complete concordance and a mutual prediction of one variable by the other is achieved using structural regression (Koch and Sporl, 2007). If the orthogonal and structural regression lines are similar, it can be concluded that both methods have comparable measurement errors. This was true for all our measurements, even for the VA1 screw hole position.

We also calculated the confidence interval limit (mean ± 1.96 SD) lines into the Bland–Altman plot. Theoretically, 95% of all actual and future measured points can be found between these lines. If this confidence interval is smaller than clinically relevant deviations, both methods are considered to be exchangeable. In nearly all considered cases these limit lines were in a range smaller than ±2 mm (after bias correction). Since screws are commonly available in steps of 2 mm, we regard both methods could interchangeable for nearly all screw types used in distal radius. Future study could assess model performance in different anatomical areas and smaller and larger screw dimensions. Potential other areas include facial fractures or facial osteotomies (due to the importance of plate placement and screw length) or correction osteotomies of the forearm or lower leg.

Both our models may be applied to a teaching environment. For example, anatomical computer models and computerized implant templates could be used within a training environment to educate surgeon when preferably selecting which osteosynthesis construct or implants, respectively. Accordingly, dedicated computer models could be generated for anatomy teaching and transferred to the 3D space applying advanced visualizations methods such as virtual reality techniques (LeBlanc et al., 2013).

This study has two main limitations. First, we used intact distal radius models for our methods. Future study should assess our methods in fractured bones. Secondly, our methods were not compared with an actual depth gauge. Future studies could compare preoperative computerized measurements with intraoperative findings.

In conclusion, we outlined CAE methods that allow for safe and enhanced anatomy assessment and exemplified their use for anatomical plate positioning and screw lengths measurement for volar plating of the distal radius. CAE methods permit non-invasive, non-destructive, and repetitive evaluations to be made. They represent valuable assessment tools when integrated into surgical fixation, implants research or teaching workflows. CAE approaches are likely to enhance training of fixation procedures and to reduce the number of post mortem specimens. Future study should assess the effect of our models on learning experience.

ACKNOWLEDGMENTS

We are grateful to those who donated their bodies to science.

REFERENCES

Bland JM, Altman DG. 1986. Statistical methods for assessing agreement between two methods of clinical measurement. Lancet 1: 307–310.

Boutroy S, Bouxsein ML, Munoz F, Delmas PD. 2005. In vivo assessment of trabecular bone microarchitecture by high-resolution peripheral quantitative computed tomography. J Clin Endocrinol Metab 90:6508–6515.

Burghardt AJ, Link TM, Majumdar S. 2011. High-resolution computed tomography for clinical imaging of bone microarchitecture. Clin Orthop Relat Res 469:2179–2193.

Buschbaum J, Fremd R, Pohlemann T, Kristen A. 2015. Computer-assisted fracture reduction: a new approach for repositioning femoral fractures and planning reduction paths. Int J Comput Assist Radiol Surg 10:149–159.

Chambers A, Mustard CA, Etches J. 2015. Trends in needlestick injury incidence following regulatory change in Ontario, Canada (2004-2012): an observational study. BMC Health Serv Res 15:127.

Chen D, Zhang Q, Deng J, Cai Y, Huang J, Li F, Xiong K. 2018. A shortage of cadavers: the predicament of regional anatomy education in mainland China. Anat Sci Educ 11:397–402.

Chung KC, Shauver MJ, Birkmeyer JD. 2009. Trends in the United States in the treatment of distal radial fractures in the elderly. J Bone Joint Surg Am 91:1868–1873.

Davis DI, Baratz M. 2010. Soft tissue complications of distal radius fractures. Hand Clin 26:229–235.

Davis KA, Burghardt AJ, Link TM, Majumdar S. 2007. The effects of geometric and threshold definitions on cortical bone metrics

assessed by in vivo high-resolution peripheral quantitative computed tomography. Calcif Tissue Int 81:364–371.
Furnstahl P, Szekely G, Gerber C, Hodler J, Snedeker JG, Harders M. 2012. Computer assisted reconstruction of complex proximal humerus fractures for preoperative planning. Med Image Anal 16:704–720.
Genant HK, Engelke K, Prevrhal S. 2008. Advanced CT bone imaging in osteoporosis. Rheumatology (Oxford) 47(Suppl 4):iv9–iv16.
Handoll HH, Elliott J. 2015. Rehabilitation for distal radial fractures in adults. Cochrane Database Syst Rev 2:CD003324.
Hopkins R, Regehr G, Wilson TD. 2011. Exploring the changing learning environment of the gross anatomy lab. Acad Med 86:883–888.
Horst TA, Jupiter JB. 2016. Stabilisation of distal radius fractures: lessons learned and future directions. Injury 47:313–319.
Kamer L, Noser H, Popp AW, Lenz M, Blauth M. 2016. Computational anatomy of the proximal humerus: an ex vivo high-resolution peripheral quantitative computed tomography study. J Orthop Translat 4:46–56.
Koch R, Sporl E. 2007. Statistical methods for comparison of two measuring procedures and for calibration: analysis of concordance, correlation and regression in the case of measuring intraocular pressure. Klin Monbl Augenheilkd 224:52–57.
LeBlanc J, Hutchison C, Hu Y, Donnon T. 2013. A comparison of orthopaedic resident performance on surgical fixation of an ulnar fracture using virtual reality and synthetic models. J Bone Joint Surg Am 95:e60–e65.
Lee LMJ, Goldman HM, Hortsch M. 2018. The virtual microscopy database-sharing digital microscope images for research and education. Anat Sci Educ 11:510–515.
Leong NL, Buijze GA, Fu EC, Stockmans F, Jupiter JB, Distal Radius Malunion Collaborative Group. 2010. Computer-assisted versus non-computer-assisted preoperative planning of corrective osteotomy for extra-articular distal radius malunions: a randomized controlled trial. BMC Musculoskelet Disord 11:282.
Melton LJ 3rd, Riggs BL, Keaveny TM, Achenbach SJ, Hoffmann PF, Camp JJ, Rouleau PA, Bouxsein ML, Amin S, Atkinson EJ, Robb RA, Khosla S. 2007. Structural determinants of vertebral fracture risk. J Bone Miner Res 22:1885–1892.
Messmer P, Matthews F, Jacob AL, Kikinis R, Regazzoni P, Noser H. 2007. A CT database for research, development and education: concept and potential. J Digit Imaging 20:17–22.
Mueller TL, Stauber M, Kohler T, Eckstein F, Muller R, van Lenthe GH. 2009. Non-invasive bone competence analysis by high-resolution pQCT: an in vitro reproducibility study on structural and mechanical properties at the human radius. Bone 44:364–371.
Noser H, Heldstab T, Schmutz B, Kamer L. 2011. Typical accuracy and quality control of a process for creating CT-based virtual bone models. J Digit Imaging 24:437–445.
Storelli DA, Bauer AS, Lattanza LL, McCarroll HR Jr. 2015. The use of computer-aided design and 3-dimensional models in the treatment of forearm malunions in children. Tech Hand Up Extrem Surg 19:23–26.
Synek A, Borgmann L, Traxler H, Huf W, Euler E, Chevalier Y, Baumbach SF. 2016. Using self-drilling screws in volar plate osteosynthesis for distal radius fractures: a feasibility study. BMC Musculoskelet Disord 17:120.
Teunis T, Bosma NH, Lubberts B, Ter Meulen DP, Ring D. 2016. Melone's concept revisited: 3D quantification of fragment displacement. J Hand Microsurg 8:27–33.
Vlachopoulos L, Schweizer A, Graf M, Nagy L, Furnstahl P. 2015. Three-dimensional postoperative accuracy of extra-articular forearm osteotomies using CT-scan based patient-specific surgical guides. BMC Musculoskelet Disord 16:336.
Voss JO, Varjas V, Raguse JD, Thieme N, Richards RG, Kamer L. 2016. Computed tomography-based virtual fracture reduction techniques in bimandibular fractures. J Craniomaxillofac Surg 44: 177–185.